Research on exotic nuclei in deformed relativistic mean-field theory plus BCS in complex momentum representation

Yu-Xuan Luo, Quan Liu,* and Jian-You Guo†
School of Physics and Optoelectronic Engineering, Anhui University, Hefei 230601, China

(Received 12 January 2023; accepted 18 August 2023; published 28 August 2023)

Study of exotic nuclei is one of the important frontiers in nuclear physics. The coupling of weakly bound states and resonant states, deformation, and pairings play important roles at the formation of exotic phenomena. To deal with these uniformly, we develop the deformed relativistic mean field theory in complex momentum representations with BCS pairings. ^{44}Mg is chosen as an illustration example. The calculated binding energy indicates that ^{44}Mg is a weakly bound nucleus. There are several broad resonant states with low orbital angular momentum near the Fermi surface, and the occupation of these levels is responsible for the halo structure in ^{44}Mg. The available density distributions suggest that ^{44}Mg is a deformed halo nucleus with prolate core and oblate halo, which agree with the deformed relativistic Hartree-Bogoliubov in continuum calculations. In particular, the role of resonances is clearly demonstrated in the halo formation, which is helpful to understand the physical mechanism of deformed exotic nuclei.

DOI: 10.1103/PhysRevC.108.024320

I. INTRODUCTION

Study of exotic nuclei is one of the important frontiers in nuclear physics, and one of the major scientific goals to develop the radionuclide beam technology over the world. Since the discovery of the first exotic nucleus ^{11}Li [1], physicists have explored many exotic phenomena in the nuclei far away from the β-stability line, which include single and double neutron (proton) halos, deformation halos, the disappearance of traditional magic numbers and the emergence of new magic numbers, energy-level inversion, novel radioactivity, new excitation modes, and so on [2,3].

In order to understand these exotic phenomena and predict new novel phenomena, physicists have proposed many theoretical models and methods. A method for incorporating the effect of the resonant continuum into Hartree-Fock+BCS equations is proposed, and the widths of resonant states are shown to have an important effect on the pairing properties of nuclei close to the drip line [4]. Combined with the complex scaling method, the few-body model presents an excellent description for light exotic nuclei [5–7]. Based on the Berggren basis, the established Gamow shell model has been effective in explaining exotic phenomena for medium mass nuclei [8–10]. To explore the novel properties of medium mass and heavy nuclei, the Gamow Hartree-Bogoliubov model was developed and the significance of coupling to the continuum was explored in Ref. [11].

Although these nonrelativistic models aforementioned are successful in describing exotic nuclei, relativistic effects are not negligible, such as the presence of spin-orbit coupling and pseudospin symmetry in realistic nuclei [12]. The self-consistent covariant density functional theory (CDFT), which includes the relativistic mean field (RMF) and relativistic Hartree-Fock (RHF) theories, is one of the most successful microscopic theoretical models in nuclear physics. It has been successful in describing not only stable nuclei, but also exotic nuclei [13–18]. The physical mechanism of the halo formation in ^{11}Li was explained successfully [19], and the possibility of the existence of a giant halo was predicted [20]. In combination with the scattering phase shift [21], the analytic continuation of the coupling constant method [22–24], the real stabilization method [25,26], the complex scaling method [27,28], the Green's function method [29–31], the roles of resonances at the formation of exotic phenomena are recognized.

In order to explore the exotic phenomena in deformed nuclei, the deformed relativistic Hartree-Bogoliubov in continuum (DRHBc) was developed [32,33]. To avoid the defect of harmonic oscillator bases, which descend too quickly with the increasing radius, the Woods-Saxon bases are proposed in the DRHBc calculations. The Woods-Saxon bases are obtained by solving Dirac equation with Woods-Saxon potential in coordinate space. The DRHBc is successful in describing deformed exotic nuclei. The deformed halo and the decoupling of the core and halo are shown clearly in the exotic nucleus ^{44}Mg [32]. A high-precision mass table in the DRHBc calculations is being constructed for even-even nuclei [34], odd-A, and odd-odd nuclei [35]. In combination with the Glauber model, the deformed halo in ^{31}Ne was reproduced in the DRHBc calculations [36]. Considering that the wave function of resonant states diverges in coordinate space, in order to avoid the limitations of the limited coordinate space for resonant states, the nuclear theory of momentum representation was developed [37]. The complex momentum representation (CMR) method can deal equally

*quanliu@ahu.edu.cn
†jianyou@ahu.edu.cn

with the bound states, resonant states, and continuous spectra. Not only narrow resonances but also broad resonances can be obtained in the CMR calculations, which is important to explore the exotic properties of weakly bound and unbound nuclei.

Due to the success of CDFT and advantages of CMR, we have established the RMF-CMR by combining RMF with CMR [37], which is applicable to describe the exotic properties of spherical nuclei. We apply the RMF-CMR to explore the pseudospin symmetry in resonant states and gain an insight into the quality of pseudospin symmetry and its dependence on the isospin and shape of potential [38,39]. To consistently handle bound states, resonant states, and couplings among them, we have developed the RMF-CMR-BCS, which successfully reproduces exotic phenomena such as halos and predicts the giant halos [40–42]. Especially, it is shown that the widths of resonant states have an important effect on the pairing properties of nuclei close to the drip line, as indicated in the RMF-rBCS calculation [4]. Considering that most known nuclei are deformed, we have developed the relativistic version of the CMR method for deformed nuclei [43], obtained the single particle resonances, and recognized the role of resonant states in the deformed exotic nuclei ^{28,29,31}F [44] and ^{75}Cr [45]. Besides the coupling of bound states and resonant states, deformation and pairings play important roles at the formation of exotic phenomena. Hence, it is necessary to develop the DRMF-CMR with BCS pairings for deformed nuclei. Since the resonance states are clearly separated from the continuum in the CMR calculation, the coupling to the resonant states can be conveniently handled with the BCS method, which is helpful to understand the physical mechanism of exotic phenomena.

Magnesium isotopes have received wide attention due to the emergence of many exotic phenomena among them. ^{37}Mg is the heaviest halo nucleus observed so far [46,47]. ^{40}Mg is the heaviest magnesium isotope detected. More than one experiment suggests that the neutron drop line of magnesium is located beyond ^{40}Mg [48,49]. The theoretical prediction of the neutron drop line is model-dependent [50]. The RMF calculations with NLSH, PK1, and NL3 suggest the drip line at ^{40}Mg [51], ^{42}Mg [33], and ^{44}Mg [52], respectively. The Skyrme-Hartree-Fock-Bogoliubov presents a weakly bound ^{44}Mg [53]. A similar conclusion was obtained in the three-body cluster model [54]. The newly developed DRHBc supports that the deformed halo structure in ^{42,44}Mg persists from the ground state to collective states [55].

In order to explore the unusual structure of deformed nuclei such as magnesium isotopes and understand the mechanism of deformed halo, we develop the DRMF-CMR-BCS. The theoretical formalism is presented in Sec. II. The numerical details and results on ^{44}Mg are stated in Sec. III. A summary is given in Sec. IV.

II. FORMALISM

To develop the DRMF-CMR-BCS, we first introduce the theoretical formalism of RMF [13,14,56]. The start point of the RMF theory is that nucleons are described as Dirac particles with interactions via mesons and photons. The effective Lagrange density takes the following form:

$$\begin{aligned}\mathcal{L} = &\bar{\psi}[i\gamma^\mu\partial_\mu - M - g_\sigma\sigma - g_\omega\gamma^\mu\omega_\mu - g_\rho\gamma^\mu\vec{\tau}\vec{\rho}_\mu]\psi \\ &- \bar{\psi}\left[\tfrac{1}{2}e\gamma^\mu(1-\tau_3)A_\mu\right]\psi + \tfrac{1}{2}\partial^\mu\sigma\partial_\mu\sigma - U(\sigma) \\ &- \tfrac{1}{4}\omega^{\mu\nu}\omega_{\mu\nu} + \tfrac{1}{2}m_\omega^2\omega^\mu\omega_\mu + \tfrac{1}{4}c_3(\omega^\mu\omega_\mu)^2 \\ &- \tfrac{1}{4}\vec{\rho}^{\mu\nu}\vec{\rho}_{\mu\nu} + \tfrac{1}{2}m_\rho^2\vec{\rho}^\mu\vec{\rho}_\mu - \tfrac{1}{4}F^{\mu\nu}F_{\mu\nu} \end{aligned} \tag{1}$$

with $U(\sigma) = \frac{1}{2}m_\sigma^2\sigma^2 + \frac{1}{3}g_2\sigma^3 + \frac{1}{4}g_3\sigma^4$. The field tensors for the mesons and photon are defined as

$$\begin{aligned}\omega^{\mu\nu} &= \partial^\mu\omega^\nu - \partial^\nu\omega^\mu, \\ \vec{\rho}^{\mu\nu} &= \partial^\mu\vec{\rho}^\nu - \partial^\nu\vec{\rho}^\mu, \\ A^{\mu\nu} &= \partial^\mu A^\nu - \partial^\nu A^\mu. \end{aligned}$$

g_σ, g_ω, and g_ρ are the coupling constants of the isoscalar-scalar σ, isoscalar-vector ω, and isovector-vector ρ mesons with the masses m_σ, m_ω, and m_ρ, respectively. The classical variational principle gives the Dirac equation

$$[\vec{\alpha}\cdot\vec{p} + \beta(M+S) + V]\psi = \varepsilon_i\psi, \tag{2}$$

for nucleons with the scalar potential $S(\vec{r})$ and vector potential $V(\vec{r})$

$$\begin{aligned}S(\vec{r}) &= g_\sigma\sigma(\vec{r}), \\ V(\vec{r}) &= g_\omega\omega^0(\vec{r}) + g_\rho\tau_3\rho^0(\vec{r}) + eA^0(\vec{r}), \end{aligned} \tag{3}$$

and the Klein-Gordon equations

$$\begin{aligned}-\nabla^2\sigma + U'(\sigma) &= -g_\sigma\rho_s, \\ -\nabla^2\omega^0 + m_\omega^2\omega^0 + c_3\omega_0^3 &= g_\omega\rho_v, \\ -\nabla^2\rho^0 + m_\rho^2\rho^0 &= g_\rho\rho_3, \\ -\nabla^2 A^0 &= e\rho_c, \end{aligned} \tag{4}$$

for mesons and photons with the source terms

$$\begin{aligned}\rho_s = \sum_{i=1}^{A}\bar{\psi}_i\psi_i,\ \rho_v = \sum_{i=1}^{A}\psi_i^\dagger\psi_i, \\ \rho_3 = \sum_{i=1}^{A}\psi_i^\dagger\tau_3\psi_i,\ \rho_c = \sum_{p=1}^{Z}\psi_p^\dagger\psi_p. \end{aligned} \tag{5}$$

For the axially deformed system with reflection symmetry, the third component of total angular momentum m_j and the parity π are good quantum numbers. The Dirac spinor can be expanded according to the spherical configurations

$$\psi_{m_j}(\vec{r}) = \frac{1}{r}\sum_{lj}\begin{pmatrix} iG^{lj}(r)Y^l_{jm_j}(\Omega_r) \\ -F^{lj}(r)Y^{\tilde{l}}_{jm_j}(\Omega_r)\end{pmatrix} \tag{6}$$

with $\tilde{l} = 2j - l$. Here, $Y^l_{jm_j}(\Omega_r)$ is the spin spherical harmonics. Putting Eq. (6) into Eq. (5), the scalar and vector densities

are obtained. The available density distributions are

$$\rho_s(r,\theta)=\sum_{\lambda}\frac{2\lambda+1}{4\pi r^2}P_\lambda(\cos\theta)\sum_{i(lj)(lj)'}v_i^2\big(G_i^{lj}G_i^{(lj)'}-F_i^{lj}F_i^{(lj)'}\big)A(\lambda,(lj)',(lj),m), \tag{7}$$

$$\rho_v(r,\theta)=\sum_{\lambda}\frac{2\lambda+1}{4\pi r^2}P_\lambda(\cos\theta)\sum_{i(lj)(lj)'}v_i^2\big(G_i^{lj}G_i^{(lj)'}+F_i^{lj}F_i^{(lj)'}\big)A(\lambda,(lj)',(lj),m) \tag{8}$$

with

$$\begin{aligned}A(\lambda,(lj)',(lj),m_j)&=\int d\Omega Y^{l}_{jm_j}(\cos\theta)^*P_\lambda(\cos\theta)Y^{l'}_{j'm_j}(\cos\theta)\\&=\int d\Omega Y^{\tilde{l}}_{jm_j}(\cos\theta)^*P_\lambda(\cos\theta)Y^{\tilde{l}'}_{j'm_j}(\cos\theta).\end{aligned} \tag{9}$$

The same as in Ref. [32], only the even number λ is considered in the multipole expansion of a function $f(\vec{r})$, i.e., $\lambda=0,2,4,\ldots$. Equations (2) and (4) are a set of coupled equations, which can be solved iteratively with a given accuracy.

To obtain the resonant states, the Dirac equation (2) is transformed into momentum representation,

$$\int d\vec{k}'\langle\vec{k}|H|\vec{k}'\rangle\psi(\vec{k}')=\varepsilon\psi(\vec{k}), \tag{10}$$

where $H=\vec{\alpha}\cdot\vec{p}+\beta(m+S(\vec{r}))+V(\vec{r})$, and $\psi(\vec{k})$ are the momentum wave functions. Similarly, the momentum wave function $\psi(\vec{k})$ to describe axially deformed nuclei is expressed as

$$\psi(\vec{k})=\psi_{m_j}(\vec{k})=\sum_{lj}\begin{pmatrix}f^{lj}(k)\phi_{ljm_j}(\Omega_k)\\ g^{lj}(k)\phi_{\tilde{l}jm_j}(\Omega_k)\end{pmatrix} \tag{11}$$

with $\phi_{ljm_j}(\Omega_k)=\sum_{m_s}\langle lm\frac{1}{2}m_s|jm_j\rangle Y_{lm}(\Omega_k)\chi_{m_s}$, where $Y_{lm}(\Omega_k)$ is spherical harmonics and χ_{m_s} is the spin wave function. Putting the wave function Eq. (11) into Eq. (10), the Dirac equation becomes

$$\begin{aligned}Mf^{lj}(k)-kg^{lj}(k)+\sum_{l'j'}\int k'^2dk'V^+(l',j',p,q,l,j,m_j,k,k')f^{l'j'}(k')=\varepsilon f^{lj}(k),\\ -kf^{lj}(k)-Mg^{lj}(k)+\sum_{l'j'}\int k'^2dk'V^-((\tilde{l})',j',p,q,\tilde{l},j,m_j,k,k')g^{l'j'}(k')=\varepsilon g^{lj}(k)\end{aligned} \tag{12}$$

with

$$\begin{aligned}&V^+(l',j',p,q,l,j,m_j,k,k')\\&=(-)^l i^{l+l'}\frac{2}{\pi}\int r^2dr[V(r)+S(r)]j_l(kr)j_{l'}(k'r)\sum_{m_s}\langle lm|Y_{pq}(\Omega_r)|l'm'\rangle\left\langle lm\frac{1}{2}m_s\middle|jm_j\right\rangle\left\langle l'm'\frac{1}{2}m_s\middle|j'm_j\right\rangle\end{aligned}$$

and

$$\begin{aligned}&V^-(\tilde{l}',j',p,q,\tilde{l},j,m_j,k,k')\\&=(-)^{\tilde{l}}i^{\tilde{l}+\tilde{l}'}\frac{2}{\pi}\int r^2dr[V(r)-S(r)]j_{\tilde{l}}(kr)j_{\tilde{l}'}(k'r)\sum_{m_s}\langle\tilde{l}\tilde{m}|Y_{pq}(\Omega_r)|\tilde{l}'\tilde{m}'\rangle\left\langle\tilde{l}\tilde{m}\frac{1}{2}m_s\middle|jm_j\right\rangle\left\langle\tilde{l}'\tilde{m}'\frac{1}{2}m_s\middle|j'm_j\right\rangle.\end{aligned}$$

For simplicity in computation, the matrix is symmetrized by $\mathbf{f}(k_a)=\sqrt{w_a}k_af(k_a)$ and $\mathbf{g}(k_a)=\sqrt{w_a}k_ag(k_a)$. After the transformation, the Dirac equation becomes

$$\begin{aligned}\sum_b\left[M\delta_{ab}\mathbf{f}^{lj}(k_b)+\sum_{l'j'}\sqrt{w_aw_b}k_ak_bV^+(l',j',p,q,l,j,m_j,k_a,k_b)\mathbf{f}^{l'j'}(k_b)-k_a\delta_{ab}\mathbf{g}^{lj}(k_b)\right]=\varepsilon\mathbf{f}^{lj}(k_a),\\ \sum_b\left[-k_a\delta_{ab}\mathbf{f}^{lj}(k_b)-M\delta_{ab}\mathbf{g}^{lj}(k_b)+\sum_{l'j'}\sqrt{w_aw_b}k_ak_bV^-(\tilde{l}',j',p,q,\tilde{l},j,m_j,k_a,k_b)\mathbf{g}^{l'j'}(k_b)\right]=\varepsilon\mathbf{g}^{lj}(k_a).\end{aligned} \tag{13}$$

Solutions of Eq. (10) become an eigenvalue problem of symmetric matrix in Eq. (13). To obtain the density distributions in the coordinate space, the wave functions are transformed into the coordinate representation with the upper and lower components as

$$G^{lj}(r)/r = -i^{l+1}\sqrt{\frac{2}{\pi}}\int k^2 dk j_l(kr) f^{lj}(k),$$
$$F^{lj}(r)/r = -i^{\tilde{l}}\sqrt{\frac{2}{\pi}}\int k^2 dk j_{\tilde{l}}(kr) g^{lj}(k). \tag{14}$$

For the weakly bound nuclei, it is necessary to consider the coupling between bound states and continuum due to pairing correlations. As the resonant states are separated clearly from the continuum in the present calculations, the BCS approximation is applicable and effective for the pairings. When the resonant states are taken into account, the pairing correlations can be dealt with the gap and particle number equations as

$$\sum_b \frac{1}{\sqrt{(\varepsilon_b-\lambda)^2+\Delta^2}} + \sum_r \int g_r(\varepsilon)\frac{1}{\sqrt{(\varepsilon-\lambda)^2+\Delta^2}}d\varepsilon = \frac{2}{G}, \tag{15}$$

$$\sum_b \left(1-\frac{\varepsilon_b-\lambda}{\sqrt{(\varepsilon_b-\lambda)^2+\Delta^2}}\right) + \sum_r \int g_r(\varepsilon)\left(1-\frac{\varepsilon-\lambda}{\sqrt{(\varepsilon-\lambda)^2+\Delta^2}}\right)d\varepsilon = N, \tag{16}$$

where $g_r(\varepsilon) = \frac{1}{\pi}\frac{\Gamma_r/2}{(\varepsilon-\varepsilon_r)^2+\Gamma_r^2/4}$. ε_b is the energy eigenvalues of H for the bound states. ε_r and Γ_r are the energy and width of resonant states of H. G is the pairing strength and N is particle number. The occupation probabilities for the bound and resonant levels can be obtained in Eqs. (15) and (16). The densities in Eqs. (7) and (8) are modified as

$$\begin{aligned}\rho_s(r,\theta) = &\sum_\lambda \frac{2\lambda+1}{4\pi r^2}P_\lambda(\cos\theta)\sum_{b(lj)(lj)'} v_b^2\left(G_b^{lj}G_b^{(lj)'} - F_b^{lj}F_b^{(lj)'}\right)A(\lambda,(lj)',(lj),m)\\ &+\sum_\lambda \frac{2\lambda+1}{4\pi r^2}P_\lambda(\cos\theta)\sum_{r(lj)(lj)'}\int g_r(\varepsilon)v_r^2 d\varepsilon\left(G_r^{lj}G_r^{(lj)'} - F_r^{lj}F_r^{(lj)'}\right)A(\lambda,(lj)',(lj),m),\end{aligned} \tag{17}$$

$$\begin{aligned}\rho_v(r,\theta) = &\sum_\lambda \frac{2\lambda+1}{4\pi r^2}P_\lambda(\cos\theta)\sum_{b(lj)(lj)'} v_b^2\left(G_b^{lj}G_b^{(lj)'} + F_b^{lj}F_b^{(lj)'}\right)A(s,(lj)',(lj),m)\\ &+\sum_\lambda \frac{2\lambda+1}{4\pi r^2}P_\lambda(\cos\theta)\sum_{r(lj)(lj)'}\int g_r(\varepsilon)v_r^2 d\varepsilon\left(G_r^{lj}G_r^{(lj)'} + F_r^{lj}F_r^{(lj)'}\right)A(\lambda,(lj)',(lj),m).\end{aligned} \tag{18}$$

The pairing correlations are handled with BCS approximation. Equations (15) and (16) are solved at a given pairing strength G or energy gap Δ. The occupation probabilities v^2 are calculated by Eqs. (15) and (16). The densities ρ_s and ρ_v are obtained by Eqs. (17) and (18), where the wave functions in the coordinate spaces $G(r)$ and $F(r)$ are computed from Eq. (14). Similarly, ρ_3 and ρ_c are obtained. The sources in Eq. (5) consist of these densities and are used to calculate the meson fields and new potentials (3). This process is repeated to the required accuracy.

III. NUMERICAL DETAILS AND RESULTS

Based on the developed DRMF-CMR-BCS formalism, we explore the ground state properties for deformed exotic nuclei with ^{44}Mg as an illustrated example. For comparison with the DRHBc calculations, the effective interaction NL3 [57] is adopted. The coupled-channel method is used to solve Eq. (10). The wave functions $f(k)$ and $g(k)$ are expanded in terms of different spherical configurations with the labels lj. The sum over lj in Eq. (11) is limited to a finite number N_c. N_c represents the number of spherical configurations adopted. In the present calculations, $N_c = 8$ is used in every block with the determined Ω^π. The momentum is truncated to $k_{\max} = 3.0$ fm^{-1}. The pairing correlations are handled with BCS approximation. The energy gap is employed by an empirical formula $\Delta = 12/\sqrt{A}$ for the neutron and proton pairings [58].

In the DRMF-CMR-BCS calculations, the available single-neutron levels in ^{44}Mg are displayed in Fig. 1. We ignore the levels that are not relevant to the problem discussed in this article, and only the 11 levels around the Fermi surface are shown in this figure. For the resonant states, the energy levels are shown with error bars. The center line and height of the bar correspond to the position and width of the level, respectively. Here, the axisymmetric deformation with reflection symmetry is considered, the third component of angular momentum Ω and the parity π are good quantum numbers, and the levels are labeled as Ω^π. For easy access to the knowledge in Fig. 1, the levels are ordered from left to right according to energy from small to large. The dotted line marks the position of chemical potential λ for neutrons. The lowest two bound levels in this figure have little effect on the exotic properties for ^{44}Mg. We mainly focus on the two weakly bound levels and the seven resonant levels, which may play an important role at the formation of exotic phenomena. For convenience, we label these levels from 1 to 9, as shown in this figure.

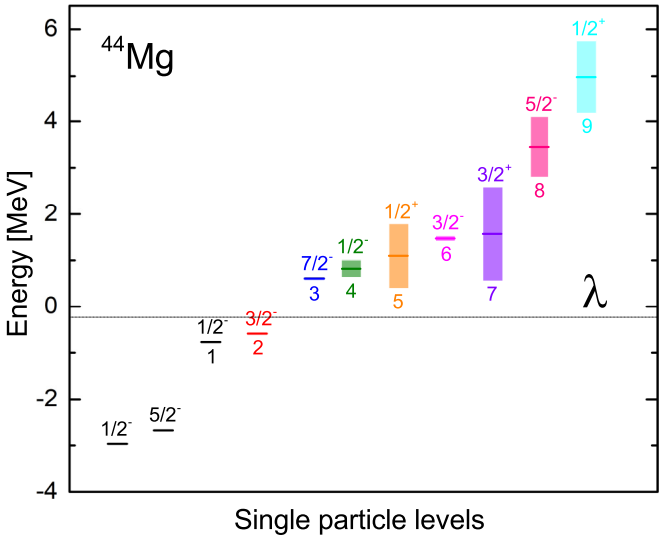

FIG. 1. The available single-neutron levels around Fermi surface including the bound states and resonant states in ^{44}Mg. For the resonant states, the energy levels are shown with error bars. The center line of the bar corresponds to the position of the energy level, and the height of the bar corresponds to the width of the energy level. The quantum numbers of angular momentum and parity are labeled as Ω^π. λ is the chemical potential marked by the dotted line, and n is the serial number of levels under consideration.

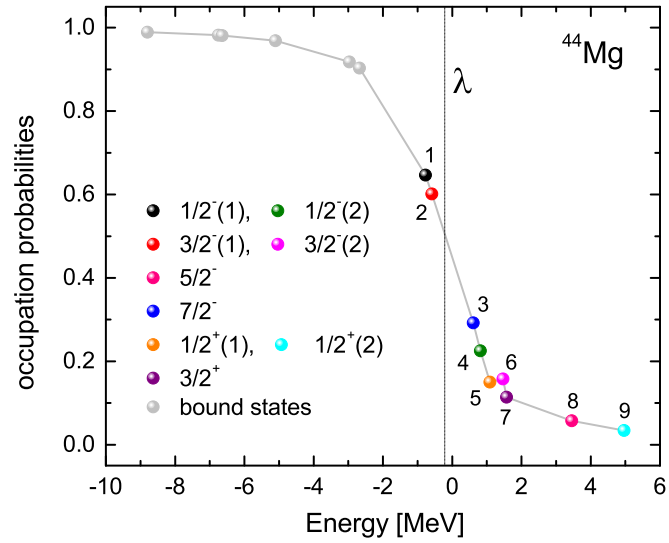

FIG. 2. The occupation probabilities of single particle levels around Fermi surface in ^{44}Mg. The relatively bound levels are denoted as gray circles. The weakly bound and resonant levels are marked as solid circles with different colors. The chemical potential λ labels the position of Fermi surface.

From Fig. 1, it can be seen that the widths are relatively small for the third ($\Omega^\pi = 7/2^-$), the fourth ($\Omega^\pi = 1/2^-$), and the sixth ($\Omega^\pi = 3/2^-$) levels. The three resonant states correspond to narrow resonances, and hold relatively long lifetimes. Comparatively, the resonant state $7/2^-$ has a longer lifetime and is similar to a quasibound state. Due to the large angular momentum and high centrifugal barrier, the neutron density distribution contributed by this level is not very diffuse. Besides these narrow resonances, there appear four broad resonances with energy below 5 MeV. As we know, the broad resonances, especially those with lower angular momentum, play an important role at the formation of the halo. For ^{44}Mg, the fifth resonant state $\Omega^\pi = 1/2^+$ and the seventh resonant state $\Omega^\pi = 3/2^+$ are the broad resonances with lower angular momentum. The occupations of the two levels result in a diffuse matter density distribution. Although the eighth resonant state $\Omega^\pi = 5/2^-$ and the ninth resonant state $\Omega^\pi = 1/2^+$ are also broad resonant states, they are far from the Fermi surface. The occupancy probabilities of the two levels are relatively small. In addition, the eighth level has a large angular momentum. These indicate that ^{44}Mg is most likely a neutron halo which is contributed by the fifth $\Omega^\pi = 1/2^+$ and the seventh $\Omega^\pi = 3/2^+$ levels. These two narrow resonances (the fourth $\Omega^\pi = 1/2^-$) and the sixth $\Omega^\pi = 3/2^-$) may have some contributions to the exotic halo structure because they have a lower centrifugal barrier.

To understand the role of resonant states at the formation of exotic properties in ^{44}Mg, in Fig. 2 we have displayed the occupation probabilities of single neutron levels for these levels in the vicinity of Fermi surface in ^{44}Mg. A vertical dotted line marks the position of the chemical potential. For all these levels, the occupation probabilities decrease gradually with increasing energy. A slight exception appears in the sixth level $\Omega^\pi = 3/2^-$. Although the energy of the level is slightly greater than that of the adjacent level $1/2^+(1)$, the occupation probabilities of the level is also slightly greater. This reason may be attributed to the width of this level $3/2^-(2)$ being much smaller than that of its adjacent level $1/2^+(1)$. Although the occupation probabilities become smaller for these levels with larger energies, the occupations of these resonant levels are not negligible. In the present calculation, the neutron number occupying these resonance levels is approximately equal to 2, which is the cause of the exotic phenomenon halo in ^{44}Mg.

To obtain an intuitive impression of exotic structure in ^{44}Mg, we have plotted the total neutron density distributions in Fig. 3(a). It can be seen that the density distributions in ^{44}Mg are very diffuse. There is a neutron halo structure in ^{44}Mg. To understand the physical mechanism of halo formation, the single neutron levels are divided into two parts. The first part consists of the deeply bound levels with energy below −2.0 MeV. The second part consists of the weakly bound and resonant levels. The energy gap between the deeply bound levels and the weakly bound levels is larger than 2.0 MeV. The neutron density distributions contributed by these deeply bound levels are displayed in Fig. 3(b), while those by the weakly bound and resonant levels are displayed in Fig. 3(c). The density distributions in Fig. 3(b) are less diffuse and correspond to "neutron core". The density distributions in Fig. 3(c) are considerably diffuse and correspond to "neutron halo". The dispersion of the total neutron density distribution come from neutron halo, i.e., the contribution of weakly bound and resonant levels. Moreover, the calculated root mean square (rms) radii of the core and the halo in ^{44}Mg are 3.94 and 8.38 fm, respectively. The rms radius of the halo

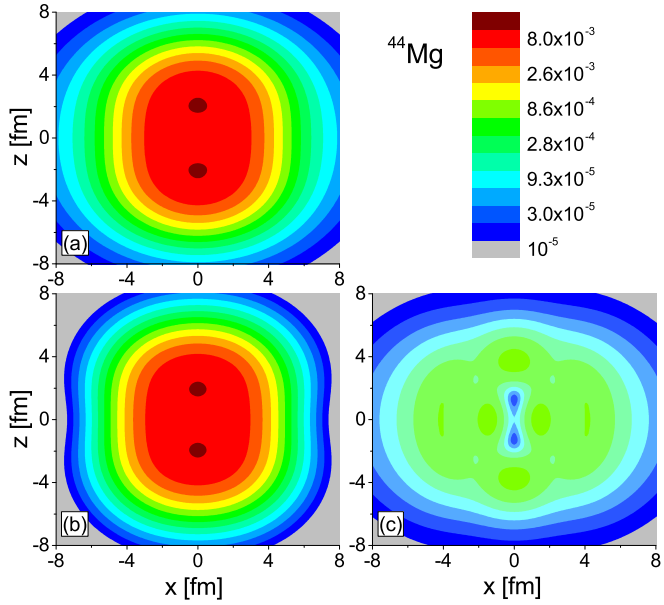

FIG. 3. The matter density distributions for neutron in ^{44}Mg. (a) displays the total neutron density distributions. (b) and (c) display the density distributions contributed by these neutrons occupying in the deeply bound levels, and those in the weakly bound and resonant levels.

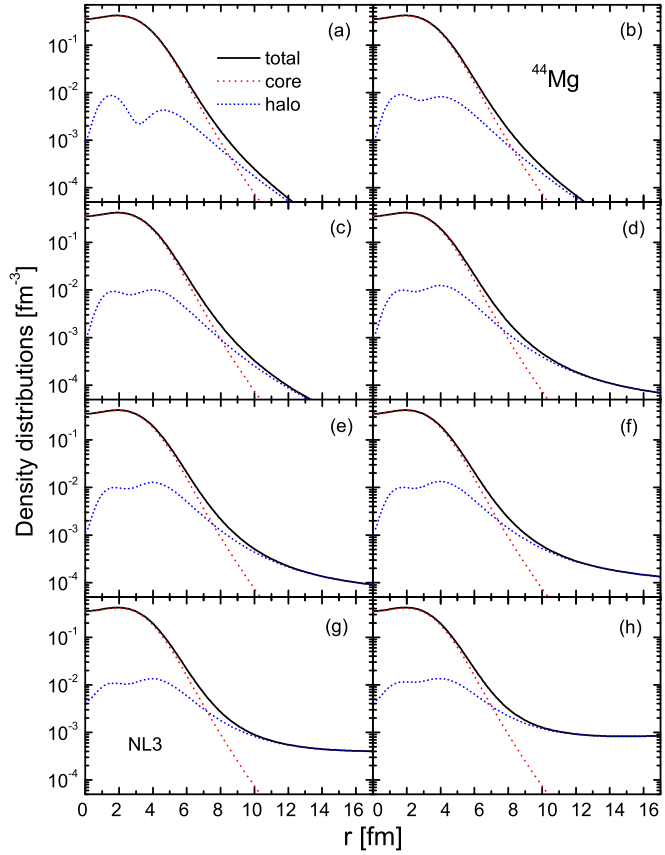

FIG. 4. The total neutron density distributions, density distributions of neutron core, and density distributions of neutron halo in ^{44}Mg, which are marked by the black solid, red dash-dot, and blue short dot lines, respectively. From (a) to (h), the resonant levels contributing neutron halo increase sequentially from near to far in terms of the distance from the real momentum axis.

is twice larger than that of the core, which is another feature of the halo. We have also observed that the density distributions of neutron core is prolate, while that of neutron halo is oblate. There is decoupling of the core and halo in ^{44}Mg, which agrees with the predication in Ref. [32].

To understand the role of resonant states at the halo formation, the total neutron density distributions, density distributions of neutron core, and density distributions of neutron halo are plotted in Fig. 4. The same as Fig. 3, in every panel, the levels are divided into two parts, the first part consists of the deeply bound levels with energy below -2.0 MeV and the second part consists of the weakly bound and the resonant levels considered. "Neutron core" corresponds to the matter distribution contributed by all the neutrons which occupy the first part of the levels. "Neutron halo" corresponds to the matter distribution contributed by all the neutrons which occupy the second part of the levels. For all the subfigures, the levels contributing to the neutron core are the same, while the levels contributing to the neutron halo are different. In Fig. 4(a), the neutron halo is contributed by the two weakly bound levels (the levels with the serial numbers 1 and 2 in Fig. 1). In Fig. 4(b), the neutron halo is contributed to by the two weakly bound levels and one resonant level (the resonant level with the serial number 3 in Fig. 1). In Fig. 4(c), the neutron halo is contributed by the two weakly bound levels and two resonant level (the two resonant levels with the serial numbers 3 and 6 in Fig. 1). Similarly, from Fig. 4(d) to Fig. 4(h), the resonant levels contributing to the neutron halo increase sequentially from near to far in terms of the distance from the real momentum axis. Until Fig. 4(h), the levels contributing to the neutron halo include the two weakly bound levels and seven resonant levels (all the resonant levels shown in Fig. 1).

From Fig. 4(a), it can be seen that all the density distributions are not very diffuse, which means that the two weakly bound energy levels do not contribute significantly to halo formation. From Fig. 4(b) to Fig. 4(h), the total neutron density distributions and the density distributions of the neutron halo become more and more diffuse, which indicates that the more resonant levels occupied by valence neutrons, the greater possibility for the formation of neutron halo. Especially, when the resonant level $1/2^+(1)$ or $3/2^+$ is considered in contributing density distributions [see Fig. 4, from (f) to (g) or from (g) to (h)], the total neutron density distributions and the density distributions of neutron halo become remarkably diffuse, which indicates that the resonant levels $1/2^+(1)$ and $3/2^+$ play important roles at the formation of neutron halo in ^{44}Mg.

As indicated in Ref. [59], there is an inherent problem in the treatment of pairing correlations with the BCS approximation. The neutron density distributions in Fig. 4(h) decrease with the increases of r in the range from $r = 0$ to $r = 12$ fm. When $r > 12$ fm, the calculated neutron density distributions decrease slowly, or even remain a small constant, with the increase of r, which means that the core is surrounded by an unphysical neutron gas. This is because the wave functions

TABLE I. The variation of binding energies with the cutoff in the tail of wave functions of resonant states. R_c represents that the tail of the wave function of resonant states is truncated from R_c. E_b is the calculated binding energy for ^{44}Mg.

R_c [fm]	E_b [MeV]	R_c [fm]	E_b [MeV]
10	−279.24788	20	−279.24487
12	−279.24492	22	−279.24487
14	−279.24481	24	−279.24487
16	−279.24484	26	−279.24487
18	−279.24485	28	−279.24487

of the resonant states are not convergent in the coordinate space. Fortunately, this defect can be cured by a cutoff in the tail of the wave functions of the resonant states [4,21]. We have checked the dependence of the calculated results on the cutoff at the tail of the wave functions of resonant states. The calculated binding energies in different cutoffs at the tail of wave functions of resonant states are listed in Table I. From Table I, it can be seen that the convergence of the calculations on the cutoff at the tail of the wave functions of resonant states is very good. With the increase of the cutoff from $R_c = 10$ fm, the change in the calculated binding energy with the increase of R_c is very small. When R_c exceeds 20 fm, the calculated binding energies remain unchanged within our current precision.

Although we recognize that resonant states are important in the formation of halos, we plotted the ratios of the density distributions of every single particle level to the total density distributions in Fig. 5 so as to find out which resonance plays a dominate role in halo ^{44}Mg. From the ratios in Fig. 5, it can be seen that the density distributions are not diffuse for the two weakly bound levels $1/2^-(1)$ and $3/2^-$ (1). The density distributions of the four broad resonant states $3/2^+$, $1/2^+(1)$, $5/2^-$, and $1/2^+(2)$ are considerably diffuse. Especially for the two broad resonant states $3/2^+$ and $1/2^+(1)$, their density

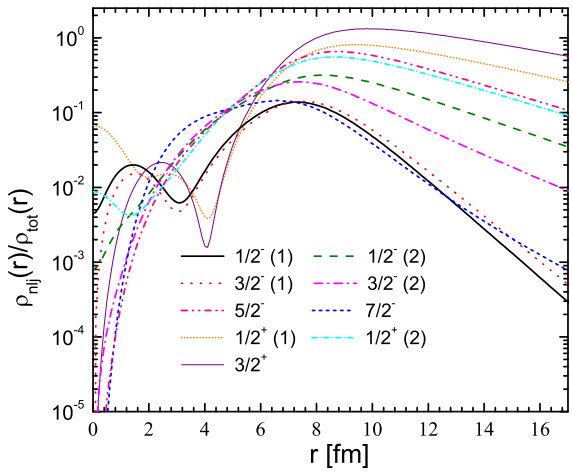

FIG. 5. The ratios of the density distributions of single particle levels to the total density distributions for the weakly bound and resonant levels in ^{44}Mg for neutrons. These levels are the same as those in Fig. 1.

distributions are very diffuse, which support the neutron halo structure in ^{44}Mg. Although the density distributions of the two broad resonant states $5/2^-$ and $1/2^+(2)$ (the eighth and ninth levels are in Fig. 2) are also diffuse, their occupancy probabilities are relatively small and their contributions to the total density are relatively small. The density distributions of the two narrow resonant levels $1/2^-$ (2) and $3/2^-(2)$ (the fourth and sixth levels are in Fig. 2) are relatively diffuse, they contribute partially to the halo because the neutron occupation probabilities of the two levels are relatively large. These indicate that the resonances, especially the broad resonances with lower angular momentum and near Fermi surface play a dominate role in the formation of the halo. The halo structure in ^{44}Mg originates mainly from the two resonant levels $3/2^+$ and $1/2^+(1)$ occupied by valence neutrons. The two broad resonant levels $5/2^-$ and $1/2^+(2)$, and the two narrow resonant levels $1/2^-(2)$ and $3/2^-(2)$ have some contributions to the halo structure in ^{44}Mg. Although the resonant state $7/2^-$ has a lower energy and a larger neutron occupation, due to the large angular momentum and high centrifugal barrier, the occupation of this level does not contribute to a diffuse neutron density distribution.

IV. SUMMARY

We have established the DRMF-CMR-BCS to explore the exotic structure for deformed nuclei. Theoretical formalism and numerical details are presented. The extremely neutron rich nucleus ^{44}Mg is chosen as an illustrate example. The single particle levels including the bound states and resonant states around the Fermi surface are obtained. There are two broad resonant states with low angular momentum near the Fermi surface, which play a dominate role at the formation of halo.

Although the calculated occupation probabilities decrease with the increasing energy, the occupations of the resonant levels are not negligible. In ^{44}Mg, the neutron number occupying in the resonant levels is approximately equal to 2, which is the cause of the formation of exotic phenomenon halo.

The available density distributions contributed to by the weakly bound and resonant levels are considerably diffuse, and are claimed as neutron halo. While those contributed to by the deeply bound levels are less diffuse, and are claimed as the neutron core. For ^{44}Mg, the neutron core is prolate, while the neutron halo is oblate. This shape decoupling phenomenon agrees with the predication in Ref. [32].

The role of every resonant state at the halo formation is explored. The density distributions contributed to by valence neutrons become more and more diffuse with the resonant levels included increasing sequentially from near to far in terms of the distance from the real momentum axis in the present calculations. The more resonant levels are occupied by valence neutrons, the more diffuse density distributions are formed.

The contribution of every resonant state to halo is compared. The resonances, especially the broad resonances with lower angular momentum and near Fermi surface, play an important role in the formation of the halo. Combining the consideration of occupation probabilities, the broad resonances

$1/2^+(1)$ and $3/2^+$ should be responsible for the halo in ^{44}Mg, while the broad resonances $5/2^-$ and $1/2^+(2)$, and the narrow resonances $1/2^-(2)$ and $3/2^-(2)$ have also some contributions to the halo structure in ^{44}Mg.

Although we have only studied ^{44}Mg, the present model is universally applicable to the neutron rich nuclei, which has been confirmed in the spherical case [40,41]. This defect in BCS approximation can be remedied by introducing a cutoff in the tail of the wave functions of the resonant states, which does not influence the conclusion that the resonant states play an important role at the formation of exotic phenomena.

ACKNOWLEDGMENTS

This work was partly supported by the National Natural Science Foundation of China under Grants No. 11935001 and 11575002, the Natural Science Foundation of Anhui Province under Grant No. 2008085MA26, Anhui project (Z010118169), Heavy Ion Research Facility in Lanzhou (HIRFL) (HIR2021PY007), the project of Key Laboratory of High Precision Nuclear Spectroscopy in Chinese Academy of Sciences, Graduate Scientific Research Project of Anhui University (YJS20210096).

[1] I. Tanihata, H. Hamagaki, O. Hashimoto, Y. Shida, N. Yoshikawa, K. Sugimoto, O. Yamakawa, T. Kobayashi, and N. Takahashi, Phys. Rev. Lett. **55**, 2676 (1985).
[2] I. Tanihata, H. Savajols, and R. Kanungo, Prog. Part. Nucl. Phys. **68**, 215 (2013).
[3] T. Nakamura, H. Sakurai, and H. Watanabe, Prog. Part. Nucl. Phys. **97**, 53 (2017).
[4] N. Sandulescu, N. Van Giai, and R. J. Liotta, Phys. Rev. C **61**, 061301(R) (2000).
[5] T. Myo, Y. Kikuchi, H. Masui, and K. Katō, Prog. Part. Nucl. Phys. **79**, 1 (2014).
[6] J. Carbonell, A. Deltuva, A. C. Fonseca, and R. Lazauskas, Prog. Part. Nucl. Phys. **74**, 55 (2014).
[7] T. Myo and K. Katō, Prog. Theor. Exp. Phys. **2020**, 12A101 (2020).
[8] N. Michel, W. Nazarewicz, M. Ploszajczak, and K. Bennaceur, Phys. Rev. Lett. **89**, 042502 (2002).
[9] N. Michel, W. Nazarewicz, M. Ploszajczak, and T. Vertse, J. Phys. G: Nucl. Part. Phys. **36**, 013101 (2009).
[10] N. Michel, J. Li, and F. Xu, Commun. Theor. Phys. **74**, 097303 (2022).
[11] N. Michel, K. Matsuyanagi, and M. Stoitsov, Phys. Rev. C **78**, 044319 (2008).
[12] H. Liang, J. Meng, and S. G. Zhou, Phys. Rep. **570**, 1 (2015).
[13] D. Vretenar, A. V. Afanasjev, G. A. Lalazissis, and P. Ring, Phys. Rep. **409**, 101 (2005).
[14] J. Meng, H. Toki, S. G. Zhou, S. Q. Zhang, W. H. Long, and L. S. Geng, Prog. Part. Nucl. Phys. **57**, 470 (2006).
[15] T. Nikšić, D. Vretenar, and P. Ring, Prog. Part. Nucl. Phys. **66**, 519 (2011).
[16] J. Meng and S. G. Zhou, J. Phys. G: Nucl. Part. Phys. **42**, 093101 (2015).
[17] J. Meng, *Relativistic Density Functional for Nuclear Structure* (World Scientific, Singapore, 2016).
[18] S. Shen, H. Liang, W. H. Long, J. Meng, and P. Ring, Prog. Part. Nucl. Phys. **109**, 103713 (2019).
[19] J. Meng and P. Ring, Phys. Rev. Lett. **77**, 3963 (1996).
[20] J. Meng and P. Ring, Phys. Rev. Lett. **80**, 460 (1998).
[21] N. Sandulescu, L. S. Geng, H. Toki, and G. C. Hillhouse, Phys. Rev. C **68**, 054323 (2003).
[22] S. S. Zhang, J. Meng, S. G. Zhou, and G. C. Hillhouse, Phys. Rev. C **70**, 034308 (2004).
[23] J. Y. Guo and X. Z. Fang, Phys. Rev. C **74**, 024320 (2006).
[24] X. D. Xu, S. S. Zhang, A. J. Signoracci, M. S. Smith, and Z. P. Li, Phys. Rev. C **92**, 024324 (2015).
[25] L. Zhang, S. G. Zhou, J. Meng, and E. G. Zhao, Phys. Rev. C **77**, 014312 (2008).
[26] Z. Z. Zhang, H. Lin, and Y. M. Mi, Mod. Phys. Lett. A **25**, 727 (2010).
[27] J. Y. Guo, X. Z. Fang, P. Jiao, J. Wang, and B. M. Yao, Phys. Rev. C **82**, 034318 (2010).
[28] Z. L. Zhu, Z. M. Niu, D. P. Li, Q. Liu, and J. Y. Guo, Phys. Rev. C **89**, 034307 (2014).
[29] T. T. Sun, S. Q. Zhang, Y. Zhang, J. N. Hu, and J. Meng, Phys. Rev. C **90**, 054321 (2014).
[30] M. Shi, J. Y. Guo, Q. Liu, Z. M. Niu, and T. H. Heng, Phys. Rev. C **92**, 054313 (2015).
[31] T. T. Sun, L. Qian, C. Chen, P. Ring, and Z. P. Li, Phys. Rev. C **101**, 014321 (2020).
[32] S. G. Zhou, J. Meng, P. Ring, and E. G. Zhao, Phys. Rev. C **82**, 011301(R) (2010).
[33] L. Li, J. Meng, P. Ring, E. G. Zhao, and S. G. Zhou, Phys. Rev. C **85**, 024312 (2012).
[34] K. Zhang, M. K. Cheoun, Y. B. Choi, P. S. Chong, J. Dong, L. Geng *et al.*, Phys. Rev. C **102**, 024314 (2020).
[35] C. Pan, M. K. Cheoun, Y. B. Choi, J. Dong, X. Du, X. H. Fan, W. Gao, L. Geng, E. Ha, X. T. He, J. Huang, K. Huang, S. Kim, Y. Kim, C. H. Lee, J. Lee, Z. Li, Z. R. Liu, Y. Ma, J. Meng *et al.*, Phys. Rev. C **106**, 014316 (2022).
[36] S. Y. Zhong, S. S. Zhang, X. X. Sun, and M. S. Smith, Sci. China: Phys., Mech. Astron. **65**, 262011 (2022).
[37] N. Li, M. Shi, J. Y. Guo, Z. M. Niu, and H. Z. Liang, Phys. Rev. Lett. **117**, 062502 (2016).
[38] X. X. Shi, Q. Liu, J. Y. Guo, and Z. Z. Ren, Phys. Lett. B **801**, 135174 (2020).
[39] Q. Liu, Y. Zhang, and J. Y. Guo, Phys. Lett. B **824**, 136829 (2020).
[40] K. M. Ding, M. Shi, J. Y. Guo, Z. M. Niu, and H. Z. Liang, Phys. Rev. C **98**, 014316 (2018).
[41] X. N. Cao, Q. Liu, Z. M. Niu, and J. Y. Guo, Phys. Rev. C **99**, 024314 (2019).
[42] X. N. Cao, K. M. Ding, M. Shi, Q. Liu, and J. Y. Guo, Phys. Rev. C **102**, 044313 (2020).
[43] Z. Fang, M. Shi, J. Y. Guo, Z. M. Niu, H. Liang, and S. S. Zhang, Phys. Rev. C **95**, 024311 (2017).
[44] Y. X. Luo, K. Fossez, Q. Liu, and J. Y. Guo, Phys. Rev. C **104**, 014307 (2021).
[45] X. W. Wang and J. Y. Guo, Phys. Rev. C **104**, 044315 (2021).
[46] M. Takechi, S. Suzuki, D. Nishimura, M. Fukuda, T. Ohtsubo, M. Nagashima *et al.*, Phys. Rev. C **90**, 061305(R) (2014).
[47] N. Kobayashi, T. Nakamura, Y. Kondo, J. A. Tostevin, Y. Utsuno, N. Aoi *et al.*, Phys. Rev. Lett. **112**, 242501 (2014).
[48] T. Baumann, A. M. Amthor, D. Bazin, B. A. Brown, C. M. Folden lll, A. Gade *et al.*, Nature (London) **449**, 1022 (2007).

[49] H. L. Crawford, P. Fallon, A. O. Macchiavelli, P. Doornenbal, N. Aoi, F. Browne *et al.*, Phys. Rev. Lett. **122**, 052501 (2019).
[50] J. Erler, N. Birge, M. Kortelainen, W. Nazarewicz, E. Olsen, A. M. Perhac *et al.*, Nature (London) **486**, 509 (2012).
[51] Z. Ren, Z. Y. Zhu, Y. H. Cai, and G. Xu, Phys. Lett. B **380**, 241 (1996).
[52] G. A. Lalazissis, D. Vretenar, P. Ring, M. Stoitsov, and L. M. Robledo, Phys. Rev. C **60**, 014310 (1999).
[53] Q. Z. Chai, J. C. Pei, N. Fei, and D. W. Guan, Phys. Rev. C **102**, 014312 (2020).
[54] Md. A. Khan, M. Hasan, S. H. Mondal, and M. Alam, Nucl. Phys. A **1015**, 122316 (2021).
[55] X. X. Sun and S. G. Zhou, Sci. Bull. **66**, 2072 (2021).
[56] P. Ring, Prog. Part. Nucl. Phys. **37**, 193 (1996).
[57] G. A. Lalazissis, J. König, and P. Ring, Phys. Rev. C **55**, 540 (1997).
[58] A. Bohr and B. R. Mottelson, *Nuclear Structure* (Benjamin, New York, 1969), Vol. I.
[59] J. Dobaczewski, H. Flocard, and J. Treiner, Nucl. Phys. A **422**, 103 (1984).